Current transport characterization and photovoltaic performance of Si nanopencil-based Schottky junction assisted with VO_x as a hole-injection layer

Mohammed Abdelhameed [a,b,c,**], Mostafa F. Abdelbar [a,b,d], A.B. El Basaty [e], Wipakorn Jevasuwan [a], Kotaro Dai [f], Kei Shinotsuka [f], Yoshihisa Hatta [f], Naoki Fukata [a,b,*]

[a] International Center for Materials Nanoarchitectonics, National Institute for Materials Science, Tsukuba, Ibaraki, 305-0044, Japan
[b] Graduate School of Pure and Applied Sciences, University of Tsukuba, Tsukuba, Ibaraki, 305-8573, Japan
[c] Faculty of Petroleum and Mining Engineering, Science and Mathematics Department, Suez University, Suez, 43518, Egypt
[d] Institute of Nanoscience and Nanotechnology, Kafrelsheikh University, Kafrelsheikh, Egypt
[e] Basic Science Department, Faculty of Technology and Education, Helwan University, Cairo, 11281, Egypt
[f] Oji Holdings Corporation, Chuo, Tokyo, 104-0061, Japan

ARTICLE INFO

Keywords:
Schottky diode
Silicon nanopencils
Vanadium oxide
Solar cells
Conduction mechanism
Barrier height

ABSTRACT

Pencil-shaped silicon nanowires (SiNPs) were utilized in Schottky junction solar cells covered by sub-stoichiometric vanadium dioxide (VO_{2-x}) to work as a hole injection layer. The asymmetry of nanopencils is responsible for their many useful properties, such as their ability to absorb and trap light over a wide spectrum. Dark current-voltage (I–V) curves for an Ag/VO_{2-x}/SiNPs/Ti/Ag Schottky junction device were measured and analyzed across a temperature range of 298–358 K. The junction parameters were calculated in terms of thermionic emission theory at different temperatures from the (I–V) curves, including the ideality factor (n) and the barrier height (φ_b), and were found to be 1.73 and 0.78 eV, respectively, at room temperature. In the forward bias regime, we found that thermionic emissions dominate at low voltages ($V \leq 0.12$ V), space-charge-limited current controlled by a single trap state dominates at middle voltages ($0.12 < V < 0.3$ V), and space-charge-limited current regulated by a distribution of trap levels dominates at high voltages ($V \geq 0.3$ V). The (C–V) measurements were used to calculate the built-in potential, which was discovered to be 0.62 eV. Unless encapsulation is provided, PEDOT:PSS/SiNPs hybrid solar cells rapidly degrade under ambient conditions, whereas VO_{2-x}/SiNPs solar cells are far more stable.

1. Introduction

In comparison to planar solar cells, nanowire (NW) architectures have various advantages for photovoltaic applications. Total light

* Corresponding author. International Center for Materials Nanoarchitectonics, National Institute for Materials Science, Tsukuba, Ibaraki, 305-0044, Japan.
** Corresponding author. International Center for Materials Nanoarchitectonics, National Institute for Materials Science, Tsukuba, Ibaraki, 305-0044, Japan
E-mail addresses: Mohammed.Abdelhameed@pme.suezuni.edu.eg (M. Abdelhameed), Fukata.Naoki@nims.go.jp (N. Fukata).

reflection on the NW sidewalls enhances the light-trapping route and charge carrier formation, according to numerical simulation and optical characteristic measurements [1–7]. Many different methods have been used to effectively create silicon nanowires (SiNWs). These include vapor-liquid-solid growth via chemical vapor deposition (CVD) [8,9], nanoimprinting followed by the Bosch process [10,11], and metal-catalyzed electroless etching (MCEE) [12,13]. The innovative synthesis approach of colloidal lithography followed by inductively coupled plasma reactive ion etching (ICP-RIE) yields high-quality pencil-shaped SiNWs that are homogeneous, asymmetrical, dense, and precisely positioned. Large-area and low-cost fabrication is difficult to achieve using traditional photolithography; hence colloidal lithography has advantages in industrial mass production. Crystalline silicon (c-Si) solar cells account for over 93% of solar cell manufacturing due to the abundance of their raw materials, durability, lack of toxicity, and high efficiency [14]. Traditional methods of synthesizing homojunction c-Si solar cells, however, necessitate the use of extremely high temperatures and a very high vacuum, which drives up production costs and increases the number of required processes. Additionally, due to the high majority carrier concentration in the highly doped area, considerable Auger recombination is typically seen [15]. Building a carrier-selective heterojunction structure by depositing thin semiconductor layers over the c-Si absorber is an alternative method of directing the light-generated electrons and holes to the appropriate electrode.

More recently, c-Si solar cells have begun using hole selective layers made of polymers such as PEDOT:PSS [16,17]. However, PEDOT:PSS/Si hybrid solar cells degrade with time due to absorption of molecular oxygen and water during outdoor operation, causing the device's overall quality to degrade and its performance to be inconsistent [18].

As a hole-transporting layer (hole-selective contact), transition metal oxides (TMOs) with a high work function are frequently utilized in organic solar cells and organic light-emitting diodes [19,20]. Vanadium oxide (VO_x) thin films show great promise due to their diverse set of desirable properties. VO_x thin films are created using a variety of synthetic processes, but the simplicity and low cost of the sol-gel process makes it very appealing. The films generated using this process may compete in quality with those formed using magnetron sputtering, spray pyrolysis, and pulsed laser deposition [21–23].

The use of VO_x in cutting-edge technologies like photovoltaics has attracted the attention of many research groups. An efficiency of 15.6% was realized by Almora et al. when V_2O_5 was utilized as the hole selective contact in a c-Si device back-reflected by a-SiC_x:H [24]. Another study investigated the insertion of VO_x as an electron-blocking layer in integrated PEDOT:PSS/Si hybrid solar cells. After optimizing the annealing temperature of the metal oxide film, the VO_x-based device was 1.6 times more efficient than a standard VO_x-free hybrid solar cell [25].

Since vanadium oxides have a wide variety of oxidation states, it is relatively difficult to obtain the required phase [26]. VO_{2-x} (B), a sub-stoichiometric vanadium dioxide, is a promising dopant-free hole-injection layer for c-Si solar cells, as shown in our recent research [27]. The sub-stoichiometry of the annealed VO_x layers results in a large density of gap states inside the bandgap, which itself is essential for hole transport.

Experimenters have shown considerable research interest in metal-semiconductor Schottky diodes because the electrical properties of their structures can be tuned by adding an interlayer between metal and semiconductor. In this situation, interface layer thickness has a significant impact on device performance, in addition to the formation and properties of the interface states. There is a lack of adequate in-depth knowledge on the transport processes and junction parameters associated with VO_x at Schottky junctions. The key parameter of the junction is the barrier height, which is a crucial characteristic that controls the behavior of electrical transport over VO_x-embedded Schottky junctions and the overall behavior of any device. The development of electrical switches and sensor devices often relies on engineering the barrier height.

In the present study, we deposited VO_{2-x} thin films using a simple solution processing method followed by vacuum annealing on pencil-shaped silicon nanowires synthesized using colloidal lithography to investigate their photovoltaic performance. This investigation also studies how the presence of a VO_{2-x} film affects the functionality of an Ag/n-Si Schottky diode. DC electrical measurements were taken as a function of both temperature and applied voltage to investigate its electronic characteristics and pinpoint its functioning conduction mechanisms. Solar cells made using VO_{2-x}/SiNPs and PEDOT:PSS/SiNPs were compared for their stability in the open air.

2. Experimental section

2.1. Silicon nanopencils fabrication technique

Utilizing a wafer of n-type CZ c-Si (100) (1.0–10.0 Ω cm, 280-μm thickness), SiNP structures were produced using colloidal lithography and ICP-RIE. Spherical colloidal silica particles measuring 300 nm in diameter were purchased from a supplier. Aminopropyltriethoxysilane or allyltrimethoxysilane was used to make the silica surface hydrophobic before the particles were immersed in the solution. After positioning the silicon substrates in a Langmuir-Blodgett trough, the silica particles were distributed in a combination of 80% chloroform and 20% ethanol on the trough's surface. Self-assembly of silica particles took place at the air-water contact, creating a monolayer. As the silicon substrate was lifted out of the sub-phase water at a rate of 5 mm/min, the monolayer of silica particles was transferred to the wafer's surface. Finally, plasma etching at an RF power of 1500 W was carried out utilizing an ICP dry etcher (Tokyo Electron ME-510 I) and CHF_3/Cl_2 gases at a pressure of 1.0 Pa. Over the course of the dry etching process, the silica was gradually eliminated, leaving behind sharp pencil tips.

2.2. Fabrication of Ag/VO_{2-x}/n-Si Schottky junction

A precursor solution was made up of 0.02 mL of vanadium(V)oxytriisopropoxide (VOTIP) diluted in 3 mL of isopropanol (IPA)

(99.9%). This solution was spun at 3000 rpm onto the substrate for 60 s. During the spin-coating process, the precursor solution converted into non-stoichiometric V_2O_5 by interacting with ambient water vapor [21]. The samples were then annealed under vacuum in a tube furnace at 400 °C and pressure of 0.15 Torr to acquire a non-stoichiometric vanadium dioxide film (VO_{2-x}) with a thickness of 15 nm. Sputtering was then used to deposit Ti/Ag (50 nm/250 nm) and Ag grid (250 nm) electrodes on the back and front of the samples.

2.3. Characterization

High-resolution field-emission scanning electron microscopy (FESEM); was used (Hitachi, SU8000) to examine the samples' morphology. The NIR spectrophotometer was employed to acquire UV–Vis–NIR reflectance spectra from 300 to 2000 nm (Jasco V-670). At 100 kHz, a semiconductor parameter analyzer was used to quantify the relationship between capacitance and voltage (*C–V*) (Agilent, Model B1500A). Observations of the fabricated junction's dark current-voltage (I–V) at a range of temperatures (298–358 K) were carried out using the last-mentioned device. Under illumination from a 1-sun air mass (AM) 1.5G Xenon lamp solar simulator, the performance of the solar cells was measured using a Keithley 2400 source meter. A Sharp solar cell made of single-crystalline silicon (BS-500) was used for the calibration.

3. Results and discussion

The SiNP structure was successfully fabricated, as shown in Fig. 1, which displays scanning electron microscopy (SEM) images of the SiNPs from a variety of angles. The SiNPs have a height of 500 nm and a pitch of 300 nm, as seen in the cross-sectional view in Fig. 1b. The reflectance data of both planar Si and SiNPs after removing their superficial oxide layer are shown in Fig. 2a. The planar surface displays the typical flat shape of Si. In comparison to the planar silicon substrate, whose reflectance varies between 75% and 30% over the wavelength range of 300–1100 nm, the SiNPs sample had significantly lower reflectance, which remained steady between zero and ten percent in the visible region due to its superior light-trapping properties. A combination of increased surface area, numerous total internal reflections inside a single nanopencil and robust light scattering within the nanopencil arrays contribute to the high *anti*-reflectivity of SiNP arrays.

Planar n-Si and n-SiNPs were deposited with 15 nm of substoichiometric vanadium dioxide (VO_{2-x}) thin film to create Ag/VO_{2-x}/n-Si/Ti/Ag Schottky junction solar cells. Lowering the barrier for hole injection at the anode/Si interface is a side effect of the incorporation of additional states at the Fermi level in the band gap of the VO_{2-x} film. This means that the shallow defect states introduced into the band gap by oxygen deficiencies play a crucial role in the transit of holes via the VO_{2-x} layer [27]. The reflectance of SiNPs covered with VO_{2-x} layer is presented in Fig. 2a, showing that the presence of 15-nm-VO_{2-x} layer with a large bandgap of 3.4 eV [27] not affect the light trapping where the reflectance remained between zero and seven percent in the visible region. The *J-V* characteristic curve of Ag/VO_{2-x}/n-Si/Ti/Ag solar cells under 100 mW cm^{-2} illumination is shown in Fig. 2b. With a short circuit current density (J_{SC}) of 23.22 mA cm^{-2}, open circuit voltage (V_{OC}) of 0.45 V, and fill factor (FF) of 0.54, the SiNPs-based device achieved a conversion efficiency of 5.6%, which outperforms the planar Si-derived device that exhibited only 4.7%. The V_{OC} value was found to be slightly lower with the SiNP device than those obtained with a planar device, suggesting that surface recombination in SiNPs-derived

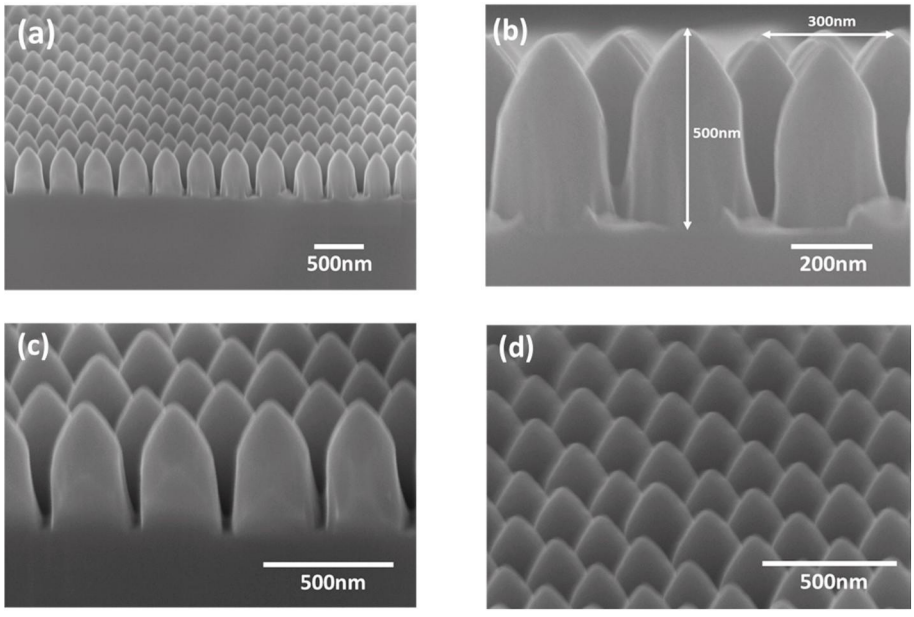

Fig. 1. (a) 30°-tilted SEM image view of SiNPs, (b) Nanopencils dimensions in a cross-sectional SEM image, (c), and (d) SiNPs at a 20° tilt.

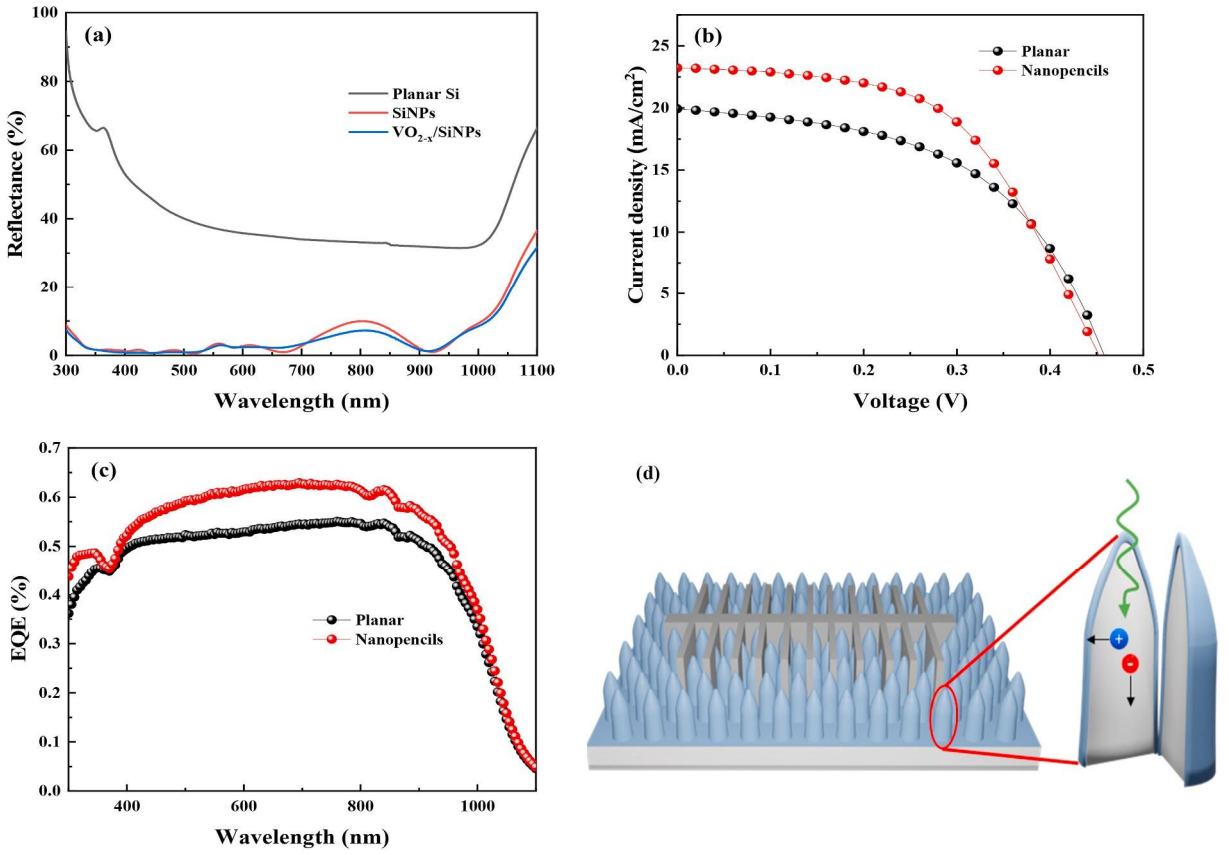

Fig. 2. (a) Reflectance spectroscopy in the UV–Vis–NIR range for planar Si, SiNPs, and VO_{x-2}/SiNPs, (b) *J-V* characteristics for Ag/VO_{2-x}/n-SiNPs and Ag/VO_{2-x}/planar n-Si solar cells, (c) EQE of VO_{x-2}/planar Si and VO_{x-2}/SiNPs, (d) Schematic view of anode/VO_{2-x}/n-SiNPs/cathode solar cell and a cross-section of VO_{2-x}/n-SiNP junction.

device is still comparable to that in the planar version. On the other hand, the solar cells with SiNPs had a much higher J_{SC} than the planar devices, since the high surface-to-volume ratio of the SiNPs allows for greater light trapping and junction area, which in turn generates more photocurrent. This suggests the metal oxide layer deposited on SiNPs has superior coverage and passivation properties to those placed on SiNWs, which were the focus of prior research [27]. Fig. 2c shows the external quantum efficiency (EQE) of the manufactured planar and nanostructured devices. The EQE results indicate the photocarrier production in 15-nm VO_{2-x}-based devices

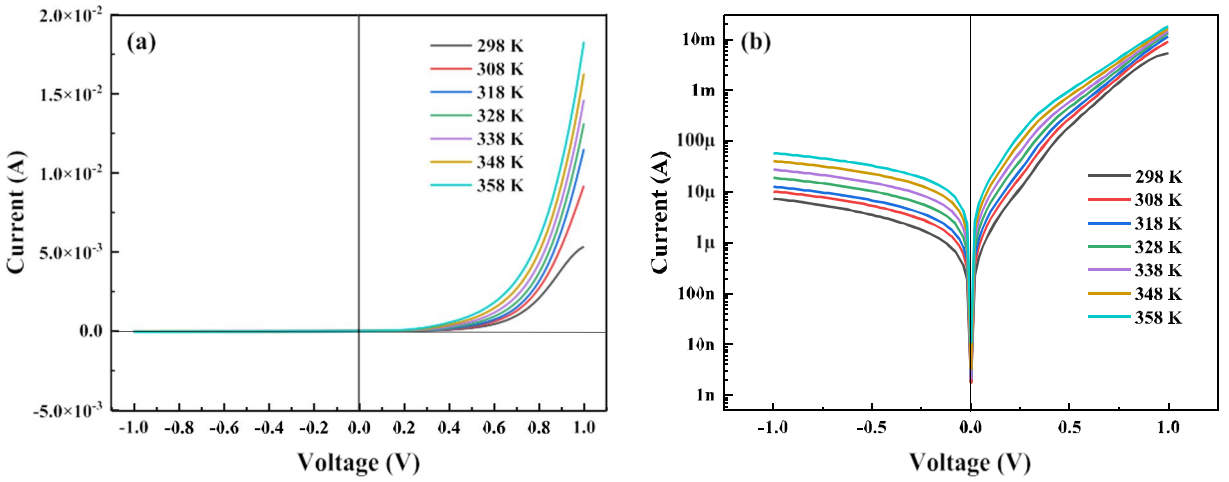

Fig. 3. (a) Ag/VO_{2-x}/n-SiNPs/Ti/Ag Schottky junction dark current-voltage characteristics at various temperatures, (b) Forward and reverse bias semi-logarithmic current–voltage (*I–V*) characteristics of the same device.

occurs throughout a wide wavelength range (300–1100 nm). The enhancement in EQE with SiNPs is markedly observed in the visible and near-infrared regions. This enhancement is attributed to the strong light trapping of the nanopencil structure which generates more photocarriers. As a result of increased junction area, enhanced carrier transport, and a significant light-trapping effect, high J_{SC} is achieved.

To understand the cell's properties, we investigated the diode properties. The temperature-dependent current-voltage characteristics of the Ag/VO_{2-x}/n-SiNPs/Ti/Ag Schottky junction diode are shown in Fig. 3, from which a substantial quantity of information pertaining to junction attributes, including the saturation current (I_0), ideality factor (n), and classification of the transport conduction mechanism, can be obtained. The electrical response displays rectification characteristics and the current increases as the temperature rises. This result indicates that Ag/VO_{2-x}/n-SiNPs Schottky junctions can be used as efficient solar cell materials because they display both p-type and n-type characteristics under the action of an external electric field. At a fixed bias, the rectification ratio (RR) is calculated as RR = $(I_f/I_r)_v$, where I_f and I_r are respectively the forward and reverse currents. At a constant biasing potential of ±1 V, the RR of the current junction increases from 314.5 to 730.9 as the temperature is raised from 298 to 358 K.

Fig. 4 shows the fluctuation of the natural logarithm of the forward current with applied voltage for the Ag/VO_{2-x}/n-SiNPs/Ti/Ag Schottky junction over the temperature range (298–358 K). The current fluctuates exponentially at relatively low applied voltages, but at high voltages, a downward curve becomes visible owing to the influence of series resistance, which comes from the contacting wires, the VO_{2-x} layer's bulk resistance, and the n-Si substrate. The data can be divided into three zones, with zone **I** occurring at $V \leq 0.12$ V, zone **II** occurring between 0.12 V and 0.3 V, and zone **III** occurring at $V \geq 0.3$ V. The barrier height and ideality factor were determined using a linear fit to the straight-line segment of the ln(I)–V plot throughout the voltage range of 0.01–0.12 V (zone **I**), as predicted from the theory of thermionic emission, which describes the current as [28,29].

$$I = I_0 \left[\exp\left(\frac{qV}{nk_BT} \right) - 1 \right] \tag{1}$$

where q is the electronic charge, V is the voltage that is being applied across the device, n is the diode ideality factor, k_B is Boltzmann's constant, T is the absolute temperature, and I_0 is the saturation current which is stated using thermionic theory as

$$I_0 = AA^*T^2 \exp\left(\frac{-q\varphi_b}{k_BT} \right) \tag{2}$$

where A represents the effective area of the device (the top electrode was used to determine that the active area of the device was 0.13 cm^{-2}), A^* represents the Richardson constant with a value of 120 A cm^{-2} K^{-2} for n-Si [30], and φ_b represents the effective barrier height when there is no bias that can be calculated using the following formula:

$$\varphi_b = \frac{k_BT}{q} ln\left(\frac{AA^*T^2}{I_0} \right) \tag{3}$$

n may be calculated using Eq. (1) as follows:

$$n = \frac{q}{k_BT} \frac{dV}{dln(I)} \tag{4}$$

Estimated values of the ideality factor and the barrier height as a function of temperature are displayed in Fig. 5a. As the

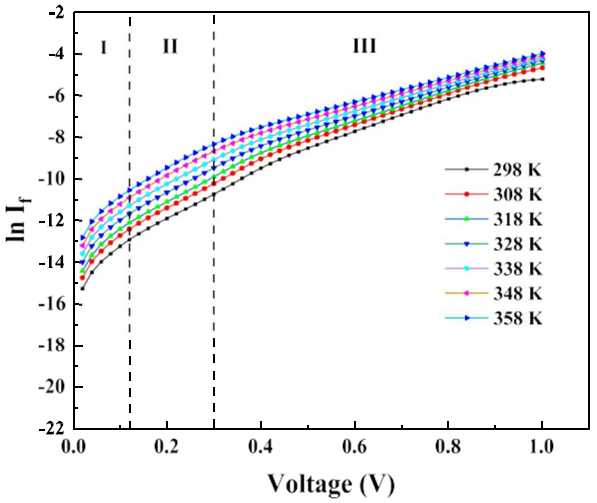

Fig. 4. Variation of (ln I_f) with forward bias voltage for VO_{2-x}/n-SiNPs Schottky junction at different temperatures.

temperature rises, the ideality factor declines as the barrier height rises. The lateral heterogeneity of the barrier height is responsible for this phenomenon. Even in the most meticulously constructed diodes, there are always variations in the barrier height [31,32]. Since electrons can overcome lower barriers at low temperatures, current transport will be mostly controlled by current passing through regions of lower barrier height. More electrons have enough energy to cross the higher barrier as the temperature rises. Thus, when temperature and bias voltage rise, the dominating barrier height will also rise [33]. As a result, the current passes through the lower barrier height and current transport is dominated by a higher ideality factor. The ideality factor is greater than 1, confirming the device's less-than-perfect performance. The high likelihood of the image-force effect [34], the existence of interface states in SiO_2 [35], and the tunneling process [36] may be possible causes of the deviation from ideal behavior.

Ideality factor and barrier height values of 1.73 and 0.78 eV were achieved at ambient temperature, which are better than those obtained by Mahato et al. [37] for an Au/V_2O_5/n-Si device (n = 2.04 and φ_b = 0.83 eV), in which the V_2O_5 layer was produced by thermal evaporation onto Si substrates. The relationship between ln (I_0/T^2) and T^{-1} is shown in Fig. 5b to verify that the thermionic emission mechanism is the working conduction mechanism in the low-voltage area. Since a straight line was produced, it is clear that the thermionic mechanism is the predominant mechanism.

The relationship between the barrier height and the ideality factor for an Ag/VO_{2-x}/n-SiNPs Schottky junction diode is shown in Fig. 5c. Straight lines are fitted to the experimental data. The value for homogeneous barrier height is obtained by extrapolating the straight line to an ideal diode with an ideality factor of 1. The homogeneous barrier height value is calculated to be 1.01 eV.

Norde suggested a means through which the barrier height of Schottky-barrier diodes may be calculated. In the extended forward bias area of the junction's I–V characteristics, the following function has been developed using a modification of Norde's method [38, 39].

$$F(V) = \frac{V}{2} - \frac{k_B T}{q} \ln\left(\frac{I(V)}{AA^* T^2}\right) \tag{5}$$

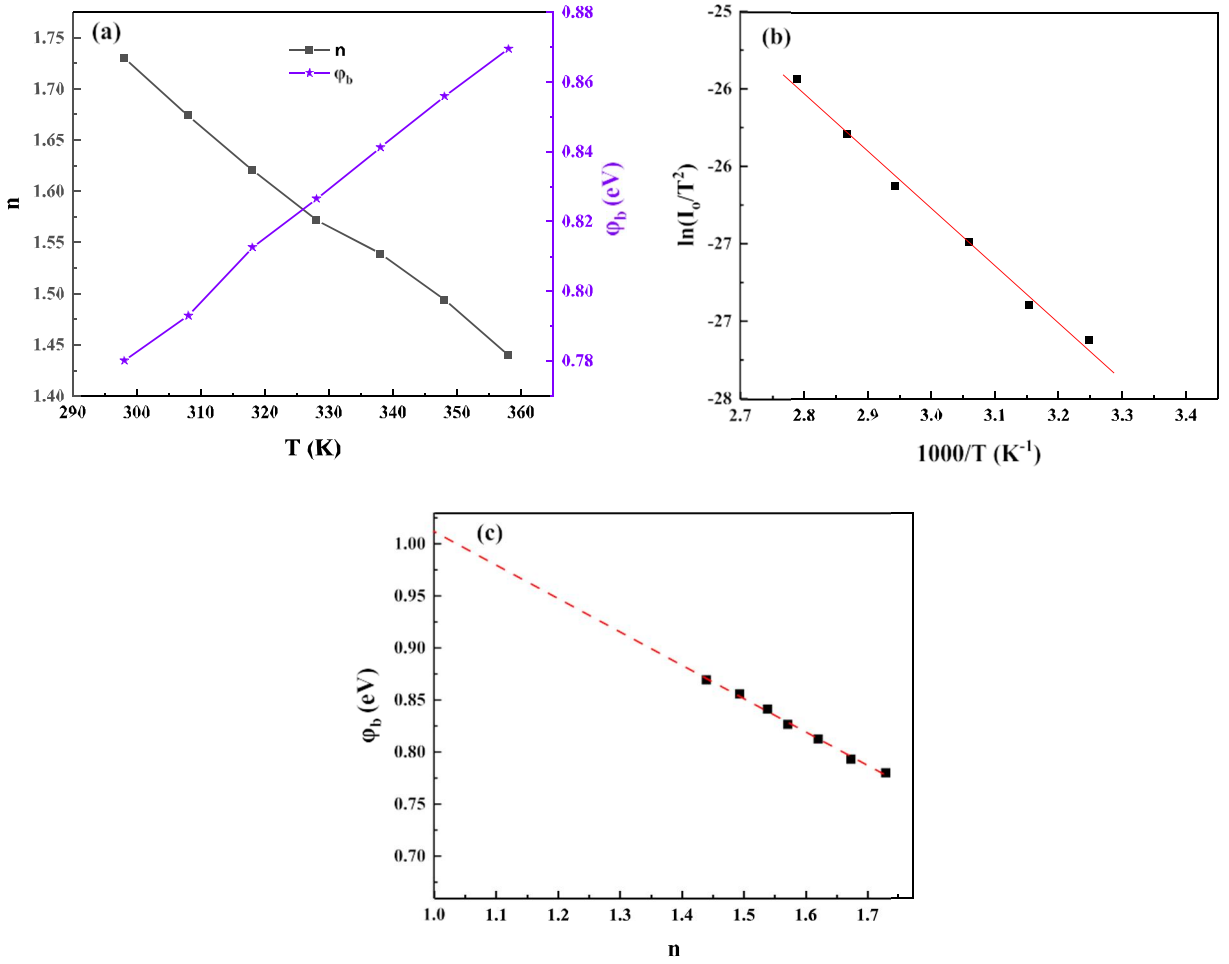

Fig. 5. (a) Temperature effects on the ideality factor (n) and barrier height (φ_b), (b) Conventional Richardson plot of Ag/VO_{2-x}/n-SiNPs/Ti/Ag diode, (c) Changes in barrier height as a function of the ideality factor.

With this approach, the barrier height may be calculated using the following formula:

$$\varphi_b = F(V_{min}) + \frac{V_{min}}{2} - \frac{k_B T}{q} \tag{6}$$

where $F(V_{min})$ is the lowest value of the Norde function $F(V)$ and V_{min} is the voltage that corresponds to the lowest value of the Norde function.

The Norde function $F(V)$ of the Ag/VO_{2-x}/n-SiNPs Schottky diode is shown plotted against the voltage (V) in Fig. 6. The values of the barrier height calculated using Norde's function at different temperatures are compared to those measured from thermionic emission and inserted in Table 1. The barrier height calculated using Norde's formula is clearly comparable to that calculated using I–V characteristics.

Fig. 7a shows the double logarithmic relationship between forward current and voltage in zone **II**. The results show a series of straight lines with slope of ~2, indicating that space-charge-limited current (SCLC) governed by a single trap state is the predominant mechanism of conduction. During the high forward biasing region, space charges are injected from n-SiNPs into the VO_{2-x} thin film, where the poor mobility of the film inhibits the charge's dynamics. The Mott-Gurney equation may be used to define the space-charge-limited-current [40,41].

$$I = \frac{9}{8}\varepsilon_r \varepsilon_0 \mu A \frac{V^2}{d^3} \frac{N_c}{N_t} \exp\left(\frac{-E_t}{k_B T}\right) \tag{7}$$

where N_c is the effective density of states at the edge of the conduction band, ε_0 is the permittivity of free space, ε_r is the relative permittivity of the semiconductor used, d is the semiconductor thickness, μ is the charge carrier mobility, and N_t is the total trap density at single energy level E_t, which is positioned below the conduction band edge. The slope of the $1/T$ vs. $\ln(I)$ plot at various forward voltages is shown in Fig. 7b, and was used to calculate E_t. An average value of 0.36 eV was found for E_t in the calculations. Herein, E_t's position is lower than that determined for Al/MoO_x/n-Si/Al device [41].

To interpret the conduction mechanism at forward voltages of ≥0.3 V (zone **III**), the linear relation between $\ln(I_f)$ and $\ln(V_f)$ of the fabricated Ag/VO_{2-x}/n-SiNPs Schottky junction diode is plotted as depicted in Fig. 8, exhibiting a slope value greater than 2. It was found that the current is dependent on the voltage in the form $I \alpha V^{2.6}$, which indicates that the SCLC, which is regulated by the distribution of trap levels, is the working mechanism in this region. Injected charge carriers can be immobilized when they fill the voids of the generated trap levels, which may be impacted by the interfacial imperfections. The current may therefore be expressed as follows [42].

$$I = \frac{q^{1-l} A \mu N_c \left(\frac{\varepsilon_r \varepsilon_0 l}{N_t (l+1)}\right)^l \left(\frac{2l+1}{l+1}\right)^l}{d^{2l+1}} V^{l+1} \tag{8}$$

where N_t denotes the density of trapping states.

The concentration of traps per unit energy at an energy E below the edge of the conduction band $P(E)$ is given by [43].

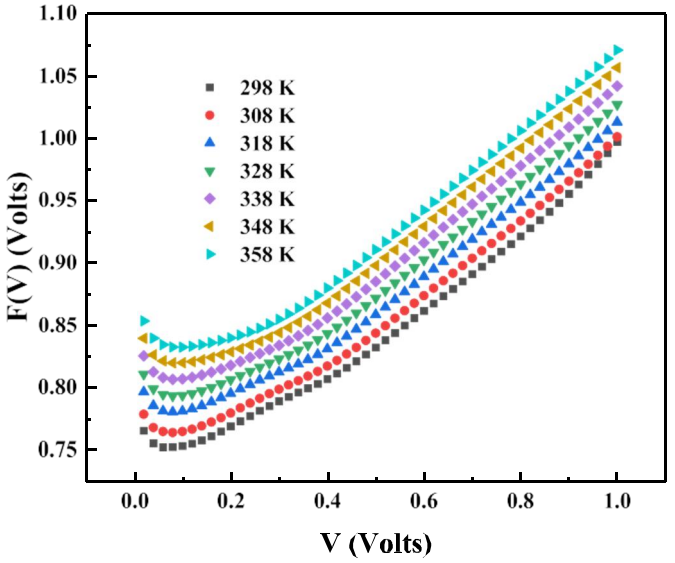

Fig. 6. Voltage dependency of $F(V)$ for Ag/VO_{2-x}/n-SiNPs/Ti/Ag diode at various temperatures.

Table 1
Electrical performance analysis of a manufactured Ag/VO_{2-x}/n-SiNPs Schottky diode.

T (K)	*I–V*		Nord's
	φ_b (eV)	n	φ_b (eV)
298	0.78	1.73	0.77
308	0.79	1.67	0.78
318	0.81	1.62	0.80
328	0.83	1.57	0.81
338	0.84	1.54	0.83
348	0.86	1.49	0.84
358	0.87	1.44	0.85

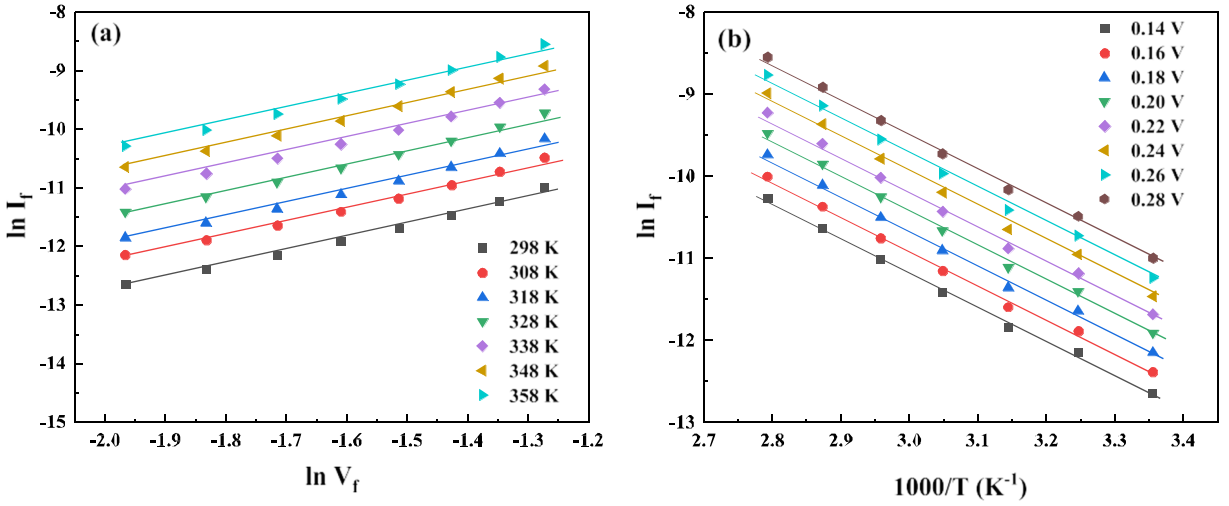

Fig. 7. (a) The Ag/VO_{2-x}/n-SiNPs/Ti/Ag diode's ln (I_f) vs ln (V_f) change with temperature in zone **II**, and (b) the temperature dependency of ln (I_f) at various voltages.

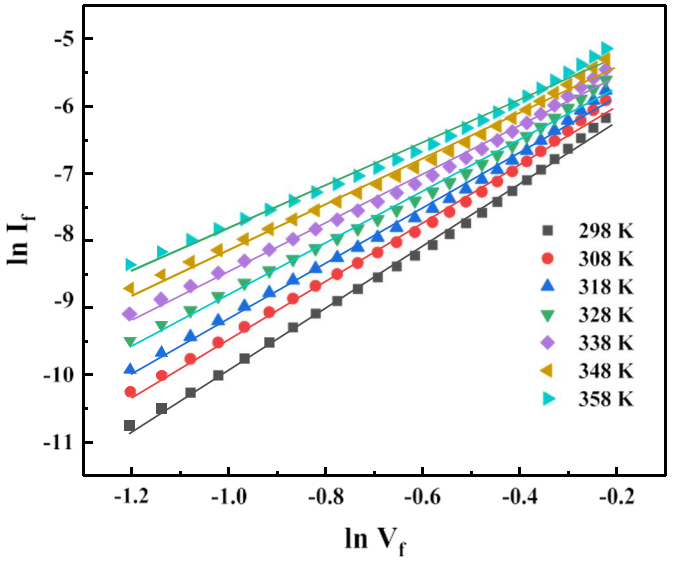

Fig. 8. The Ag/VO_{2-x}/n-SiNPs/Ti/Ag diode's ln (I_f) vs. ln (V_f) change with temperature in zone **III**.

$$P(E) = P_0 \exp\left(\frac{-E}{k_B T l}\right) \tag{9}$$

where P_0 denotes the trap density per unit energy range below the conduction band edge. Integrating Eq. (9) yields a rough estimate of the overall trap density, N_t, which is then given by [44].

$$N_t = P_0 k_B T l \tag{10}$$

At room temperature, the N_t values are calculated from Eq. (8), and average 2.04×10^{20} m^{-3}. By substituting in Eq. (10), the average value of P_0 is approximately 4.96×10^{21} $eV^{-1}m^{-3}$.

Fig. 9a displays the Mott-Schottky ($1/C^2$–V) plot for the Ag/VO_{2-x}/n-SiNPs Schottky diode at frequency 100 kHz at room temperature. It is assumed that the capacitance is related to voltage as [45].

$$\frac{1}{C^2} = \frac{2(V_{bi} - V)}{qN_D\varepsilon_r\varepsilon_0} \tag{11}$$

where N_D is the doping density (around 10^{15} cm^{-3} for 1.0–10.0 Ω cm n-Si [46]). Using the x-intercept of the $1/C^2$–V plot, the built-in potential (V_{bi}) of the fabricated diode was determined to be 0.62 eV. The depletion region width (W_D) is determined by the following equation [47].

$$W_D = \sqrt{\frac{2\varepsilon_r\varepsilon_0 V_{bi}}{qN_D}} \tag{12}$$

The depletion width is estimated to be close to 896 nm, which is wider than the SiNP length (500 nm). All majority carriers are depleted from the nanopencil structure, and as a result, the nanopencil structure facilitates a more effective collection of light-generated minority carriers over a limited collection length than is possible with a planar structure that is thick enough to produce full light absorption across the solar spectrum. The energy band diagram for Ag/VO_{2-x}/n-SiNPs/Ti/Ag solar cell is presented in Fig. 9b, showing the parameters calculated from the diode investigations.

The stability of the Ag/VO_{2-x}/n-SiNPs device was investigated and compared with that of the Ag/PEDOT:PSS/n-SiNPs hybrid solar cell. A PCE reading was taken daily for a month at 60% humidity and room temperature. The normalized PCEs over time for the two devices are shown in Fig. 10. Due to increases in V_{OC} and FF as well as decreases in R_S, the VO_{2-x} device's normalized PCE demonstrated a more consistent performance than PEDOT:PSS, with its normalized PCE improved by around 6%. The work function of the silver electrode increased from 4.3 eV to 5.0 eV when the silver layer was oxidized, which improves FF and the performance of the solar cell [48,49]. After 72 h, a slight increase of about 5 mV was seen in V_{OC}, possibly attributable to the decrease in saturation current that accompanies the oxidation of silver electrodes in air. While the PEDOT:PSS device should have demonstrated a similar rise, the rapid degradation of the fabricated hybrid cell overtook the improvement attained by the electrode. Four days after manufacturing, the PEDOT:PSS-based device had lost more than 65% of its PCE, and a 73% drop in FF was noted, indicating this rapid loss in PCE to be mainly attributable to this drop in FF. The degradation was attributed to oxygen uptake, which causes PEDOT:PSS phase separation, as explained by Norrman et al. [18] Ultimately, a loss of 85% in PCE was observed in the PEDOT:PSS device after 30 days, making it abundantly clear that the VO_x device was superior to the hybrid device.

4. Conclusion

In summary, a Ag/VO_{2-x}/n-SiNPs Schottky solar cell was made by depositing a 15 nm-thick VO_{2-x} layer on an n-SiNP substrate which exhibited a PCE of 5.6%. The SiNPs-based device outperformed its planar equivalent in solar cell performance due to its strong light-trapping feature. At temperatures of between 298 and 358 K, the I–V-T curve demonstrated excellent Ag/VO_{2-x}/n-SiNPs diode performance, with substantial RR values of 314.5–730.9. Thermionic emission, space-charge-limited-current controlled by a single trap state, and space-charge-limited-current regulated by a distribution of trap levels are the three primary transport mechanisms discovered in the forward bias regime based on the I–V-T measurements. Capacitance-voltage measurements at 100 kHz provide details on the depletion layer on the silicon side, with V_{bi} determined to be 0.62 V and the depletion width predicted to be roughly 900 nm. The SiNPs-based solar cells using VO_{2-x} films showed much higher stability than those with PEDOT:PSS film.

Credit author statement

Mohammed Abdelhameed: Methodology, Validation, Investigation, Writing - Original Draft. **Mostafa F. Abdelbar**: Validation, Investigation. **A. B. El Basaty**: Investigation, Writing - Review & Editing. **Wipakorn Jevasuwan**: Writing - Review & Editing. **Kotaro Dai**: Investigation. **Kei Shinotsuka**: Investigation. **Yoshihisa Hatta**: Investigation. **Naoki Fukata**: Conceptualization, Resources, Writing -Review & Editing, Supervision, Funding acquisition.

Declaration of competing interest

The authors declare that they have no known competing financial interests or personal relationships that could have appeared to influence the work reported in this paper.

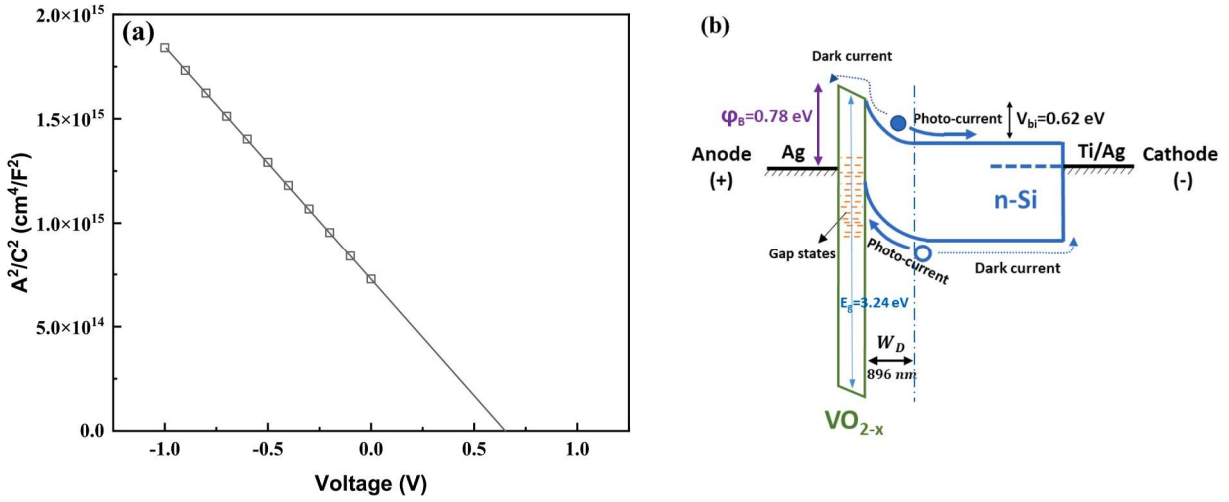

Fig. 9. (a) Mott-Schottky capacitance-voltage characteristics for Ag/VO_{2-x}/n-SiNPs device, (b) Energy band diagram for Ag/VO_{2-x}/n-SiNPs/Ti/Ag solar cell.

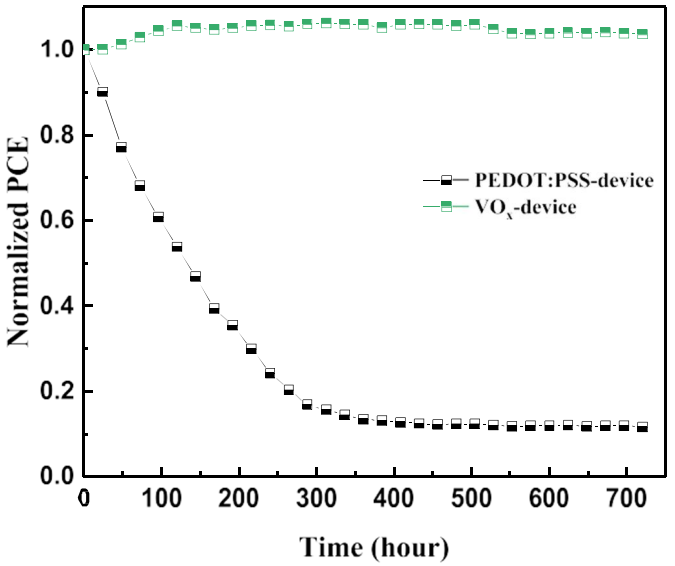

Fig. 10. Normalized power-conversion efficiency (PCE) degradation for VO_{x-2}/n-SiNPs and PEDOT:PSS/n-SiNPs solar cells.

Data availability

No data was used for the research described in the article.

Acknowledgment

This work was supported by JSPS Kakenhi Grants Nos. 26246021 and 26600049, and by the World Premier International Research Center Initiative (WPI Initiative), MEXT, Japan. Mohammed Abdelhameed is funded by a full scholarship from the Ministry of Higher Education of the Arab Republic of Egypt to support his PhD studies.

References

[1] A.I. Hochbaum, P. Yang, Semiconductor nanowires for energy conversion, Chem. Rev. 110 (2010) 527–546, https://doi.org/10.1021/cr900075v.
[2] M.D. Kelzenberg, S.W. Boettcher, J.A. Petykiewicz, D.B. Turner-Evans, M.C. Putnam, E.L. Warren, J.M. Spurgeon, R.M. Briggs, N.S. Lewis, H.A. Atwater, Enhanced absorption and carrier collection in Si wire arrays for photovoltaic applications, Nat. Mater. 9 (2010) 239–244, https://doi.org/10.1038/nmat2635.
[3] K.Q. Peng, S.T. Lee, Silicon nanowires for photovoltaic solar energy conversion, Adv. Mater. 23 (2011) 198–215, https://doi.org/10.1002/adma.201002410.

[4] J. Li, H. Yu, Y. Li, Aligned Si nanowire-based solar cells, Nanoscale 3 (2011) 4888–4900, https://doi.org/10.1039/C1NR10943J.
[5] N. Fukata, T. Subramani, W. Jevasuwan, M. Dutta, Y. Bando, Functionalization of silicon nanostructures for energy-related applications, Small 13 (2017) 1–13, https://doi.org/10.1002/smll.201701713.
[6] G. Jia, J. Plentz, I. Ho¨ger, J. Dellith, A. Dellith, F. Falk, Core–shell diodes for particle detectors, J. Phys. D Appl. Phys. 49 (2016), 065106, https://doi.org/10.1088/0022-3727/49/6/065106.
[7] M.F. Abdelbar, M. El-Kemary, N. Fukata, Downshifting of highly energetic photons and energy transfer by Mn-doped perovskite CsPbCl3 nanocrystals in hybrid organic/silicon nanostructured solar cells, Nano Energy 77 (2020), 105163, https://doi.org/10.1016/j.nanoen.2020.105163.
[8] N. Fukata, M. Mitome, T. Sekiguchi, Y. Bando, M. Kirkham, J.-I. Hong, Z.L. Wang, R.L. Snyder, Characterization of impurity doping and stress in Si/Ge and Ge/Si core–shell nanowires, ACS Nano 6 (2012) 8887–8895, https://doi.org/10.1021/nn302881w.
[9] A.I. Hochbaum, R. Fan, R. He, P. Yang, Controlled growth of Si nanowire arrays for device integration, Nano Lett. 5 (2005) 457–460, https://doi.org/10.1021/nl047990x.
[10] W. Jevasuwan, K.C. Pradel, T. Subramani, J. Chen, T. Takei, K. Nakajima, Y. Sugimoto, N. Fukata, Diffused back surface field formation in combination with two-step H 2 annealing for improvement of silicon nanowire-based solar cell efficiency, Jpn. J. Appl. Phys. 56 (2017), 04CP01, https://doi.org/10.7567/JJAP.56.04CP01.
[11] X. Zhang, W. Jevasuwan, Y. Sugimoto, N. Fukata, Controlling catalyst-free formation and hole gas accumulation by fabricating Si/Ge core-shell and Si/Ge/Si core-double shell nanowires, ACS Nano 13 (2019) 13403–13412, https://doi.org/10.1021/acsnano.9b06821.
[12] M. Abdelhameed, W. Jevasuwan, T. Subramani, J. Chen, N. Fukata, Nano Energy Efficiency enhancement of Si nanostructure hybrid solar cells by optimizing non-radiative energy transfer from Si quantum dots, Nano Energy 82 (2021), 105728, https://doi.org/10.1016/j.nanoen.2020.105728.
[13] M. Otto, M. Algasinger, H. Branz, B. Gesemann, T. Gimpel, K. Füchsel, T. K¨asebier, S. Kontermann, S. Koynov, X. Li, V. Naumann, J. Oh, A.N. Sprafke, J. Ziegler, M. Zilk, R.B. Wehrspohn, Black silicon photovoltaics, Adv. Opt. Mater. 3 (2015) 147–164, https://doi.org/10.1002/adom.201400395.
[14] P.-J. Ribeyron, Crystalline silicon solar cells: better than ever, Nat. Energy 2 (2017), 17067, https://doi.org/10.1038/nenergy.2017.67.
[15] A. Richter, S.W. Glunz, F. Werner, J. Schmidt, A. Cuevas, Improved quantitative description of Auger recombination in crystalline silicon, Phys. Rev. B 86 (2012), 165202, https://doi.org/10.1103/PhysRevB.86.165202.
[16] Z. Sun, Y. He, B. Xiong, S. Chen, M. Li, Y. Zhou, Y. Zheng, K. Sun, C. Yang, Strategien zur Steigerung der Leistung von PEDOT:PSS/Si-Hybrid-Solarzellen, Angew. Chemie. 133 (2021) 5092–5112, https://doi.org/10.1002/ange.201910629.
[17] T. Subramani, J. Chen, Y.L. Sun, W. Jevasuwan, N. Fukata, High-efficiency silicon hybrid solar cells employing nanocrystalline Si quantum dots and Si nanotips for energy management, Nano Energy 35 (2017) 154–160, https://doi.org/10.1016/j.nanoen.2017.03.037.
[18] K. Norrman, M.V. Madsen, S.A. Gevorgyan, F.C. Krebs, Degradation patterns in water and oxygen of an inverted polymer solar cell, J. Am. Chem. Soc. 132 (2010) 16883–16892, https://doi.org/10.1021/ja106299g.
[19] H. You, Y. Dai, Z. Zhang, D. Ma, Improved performances of organic light-emitting diodes with metal oxide as anode buffer, J. Appl. Phys. 101 (2007) 1–4, https://doi.org/10.1063/1.2430511.
[20] J. Meyer, K. Zilberberg, T. Riedl, A. Kahn, Electronic structure of Vanadium pentoxide: an efficient hole injector for organic electronic materials, J. Appl. Phys. 110 (2011), https://doi.org/10.1063/1.3611392.
[21] N. O¨zer, Electrochemical properties of sol-gel deposited vanadium pentoxide films, Thin Solid Films 305 (1997) 80–87, https://doi.org/10.1016/S0040-6090(97)00086-2.
[22] S. Beke, S. Giorgio, L. Koro¨si, L. Na´nai, W. Marine, Structural and optical properties of pulsed laser deposited V2O5 thin films, Thin Solid Films 516 (2008) 4659–4664, https://doi.org/10.1016/J.TSF.2007.08.113.
[23] A. Bouzidi, N. Benramdane, A. Nakrela, C. Mathieu, B. Khelifa, R. Desfeux, A. Da Costa, First synthesis of vanadium oxide thin films by spray pyrolysis technique, Mater. Sci. Eng. B. 95 (2002) 141–147, https://doi.org/10.1016/S0921-5107(02)00224-6.
[24] O. Almora, L.G. Gerling, C. Voz, R. Alcubilla, J. Puigdollers, G. Garcia-Belmonte, Superior performance of V2O5 as hole selective contact over other transition metal oxides in silicon heterojunction solar cells, Sol. Energy Mater. Sol. Cells 168 (2017) 221–226, https://doi.org/10.1016/j.solmat.2017.04.042.
[25] C.Y. Chen, T.C. Wei, P.H. Hsiao, C.H. Hung, Vanadium oxide as transparent carrier-selective layer in silicon hybrid solar cells promoting photovoltaic performances, ACS Appl. Energy Mater. 2 (2019) 4873–4881, https://doi.org/10.1021/acsaem.9b00565.
[26] R. Wang, T. Katase, K.K. Fu, T. Zhai, J. Yang, Q. Wang, H. Ohta, N. Koch, S. Duhm, Oxygen vacancies allow tuning the work function of vanadium dioxide, Adv. Mater. Interfaces. 5 (2018) 1–7, https://doi.org/10.1002/admi.201801033.
[27] M. Abdelhameed, M.F. Abdelbar, M. Esmat, Nano Energy Hole-injection role of solution-processed thermally treated VO x thin films in Si nanowire-based solar cells, Nano Energy 99 (2022), 107373, https://doi.org/10.1016/j.nanoen.2022.107373.
[28] S.M. Sze, K.K. Ng, Physics of Semiconductor Devices, John Wiley & Sons, Inc., Hoboken, NJ, USA, 2006, https://doi.org/10.1002/0470068329.
[29] R.T. Tung, Recent advances in Schottky barrier concepts, Mater. Sci. Eng. R Reports. 35 (2001) 1–138, https://doi.org/10.1016/S0927-796X(01)00037-7.
[30] T. Tunç, S¸. Altindal, I˙. Uslu, I˙. Do¨kme, H. Uslu, Temperature dependent current-voltage (I-V) characteristics of Au/n-Si (111) Schottky barrier diodes with PVA (Ni,Zn-doped) interfacial layer, Mater. Sci. Semicond. Process. 14 (2011) 139–145, https://doi.org/10.1016/j.mssp.2011.01.018.
[31] W.P. Leroy, K. Opsomer, S. Forment, R.L. Van Meirhaeghe, The barrier height inhomogeneity in identically prepared Au/n-GaAs Schottky barrier diodes, Solid State Electron. 49 (2005) 878–883, https://doi.org/10.1016/j.sse.2005.03.005.
[32] R.F. Schmitsdorf, Explanation of the linear correlation between barrier heights and ideality factors of real metal-semiconductor contacts by laterally nonuniform Schottky barriers, J. Vac. Sci. Technol. B Microelectron. Nanom. Struct. 15 (1997) 1221, https://doi.org/10.1116/1.589442.
[33] V. Janardhanam, H.-K. Lee, K.-H. Shim, H.-B. Hong, S.-H. Lee, K.-S. Ahn, C.-J. Choi, Temperature dependency and carrier transport mechanisms of Ti/p-type InP Schottky rectifiers, J. Alloys Compd. 504 (2010) 146–150, https://doi.org/10.1016/j.jallcom.2010.05.074.
[34] S.M. Lee, Y. Jang, J. Jung, J.H. Yum, E.S. Larsen, S.Y. Lee, H. Seo, C.W. Bielawski, H.-D. Lee, J. Oh, Crystalline BeO grown on 4H-SiC via atomic layer deposition: band alignment and interface defects, ACS Appl. Electron. Mater. 1 (2019) 617–624, https://doi.org/10.1021/acsaelm.9b00098.
[35] I˙.Y. Erdog˘an, O¨. Güllü, Silicon MIS diodes with Cr2O3 nanofilm: optical, morphological/structural and electronic transport properties, Appl. Surf. Sci. 256 (2010) 4185–4191, https://doi.org/10.1016/j.apsusc.2010.01.122.
[36] J. Lee, T. Uhrmann, T. Dimopoulos, H. Bruckl, J. Fidler, TEM study on diffusion process of NiFe Schottky and MgO/NiFe tunneling diodes for spin injection in silicon, IEEE Trans. Magn. 46 (2010) 2067–2069, https://doi.org/10.1109/TMAG.2010.2040594.
[37] S. Mahato, D. Biswas, L.G. Gerling, C. Voz, J. Puigdollers, Analysis of temperature dependent current-voltage and capacitance-voltage characteristics of an Au/V 2 O 5/n -Si Schottky diode, AIP Adv. 7 (2017), 085313, https://doi.org/10.1063/1.4993553.
[38] H. Norde, A modified forward I - V plot for Schottky diodes with high series resistance, J. Appl. Phys. 50 (1979) 5052–5053, https://doi.org/10.1063/1.325607.
[39] I.M. Soliman, M.M. El-Nahass, B.A. Khalifa, Characterization and photovoltaic performance of organic device based on AlPcCl/p-Si heterojunction, Synth. Met. 209 (2015) 55–59, https://doi.org/10.1016/j.synthmet.2015.06.016.
[40] P.A. Leighton, Electronic processes in ionic crystals (Mott, N. F.; gurney, R. W.), J. Chem. Educ. 18 (1941) 249, https://doi.org/10.1021/ed018p249.1.
[41] M.M. Makhlouf, H. Khallaf, M.M. Shehata, Impedance spectroscopy and transport mechanism of molybdenum oxide thin films for silicon heterojunction solar cell application, Appl. Phys. A. 128 (2022) 98, https://doi.org/10.1007/s00339-021-05215-z.
[42] M.A. Lampert, Volume-controlled current injection in insulators, Reports Prog. Phys. 27 (1964) 307, https://doi.org/10.1088/0034-4885/27/1/307.
[43] S¸. Karatas¸, C. Temirci, M. Çakar, A. Türüt, Temperature dependence of the current–voltage characteristics of the Al/Rhodamine-101/p-Si(100) contacts, Appl. Surf. Sci. 252 (2006) 2209–2216, https://doi.org/10.1016/j.apsusc.2005.03.222.
[44] E.H. Rhoderick, Metal-semiconductor contacts, IEE Proc. I Solid State Electron Devices 129 (1982) 1, https://doi.org/10.1049/ip-i-1.1982.0001.
[45] J. Tang, K.W. Kemp, S. Hoogland, K.S. Jeong, H. Liu, L. Levina, M. Furukawa, X. Wang, R. Debnath, D. Cha, K.W. Chou, A. Fischer, A. Amassian, J.B. Asbury, E. H. Sargent, Colloidal-quantum-dot photovoltaics using atomic-ligand passivation, Nat. Mater. 10 (2011) 765–771, https://doi.org/10.1038/nmat3118.
[46] G. Ma, R. Du, Y. Cai, C. Shen, X. Gao, Y. Zhang, F. Liu, W. Shi, Solar Energy Materials and Solar Cells Improved power conversion e ffi ciency of silicon nanowire solar cells based on transition metal oxides, Sol. Energy Mater. Sol. Cells 193 (2019) 163–168, https://doi.org/10.1016/j.solmat.2019.01.010.

[47] P.R. Brown, R.R. Lunt, N. Zhao, T.P. Osedach, D.D. Wanger, L.-Y. Chang, M.G. Bawendi, V. Bulovi´c, Improved current extraction from ZnO/PbS quantum dot heterojunction photovoltaics using a MoO 3 interfacial layer, Nano Lett. 11 (2011) 2955–2961, https://doi.org/10.1021/nl201472u.
[48] C.P. Chen, Y.D. Chen, S.C. Chuang, High-performance and highly durable inverted organic photovoltaics embedding solution-processable vanadium oxides as an interfacial hole-transporting layer, Adv. Mater. 23 (2011) 3859–3863, https://doi.org/10.1002/adma.201102142.
[49] D. Wang, N.K. Elumalai, M.A. Mahmud, M. Wright, M.B. Upama, K.H. Chan, C. Xu, F. Haque, G. Conibeer, A. Uddin, V2O5 -Pedot, PSS bilayer as hole transport layer for highly efficient and stable perovskite solar cells, Org. Electron. 53 (2018) 66–73, https://doi.org/10.1016/j.orgel.2017.10.034.